



Multi-energy source (MES) configuration for bead shape control in wire-based directed energy deposition (w-DED)

Guangyu Chen^{*}, Stewart Williams, Jialuo Ding, Chong Wang, Wojciech Suder

Welding Engineering and Laser Processing Centre, Cranfield University, Bedford MK43 0AL, United Kingdom

ARTICLE INFO

Associate Editor: Adam Thomas Clare

Keywords:

Wire additive manufacture
Wire based directed energy deposition
Multi-energy source
Scanning laser

ABSTRACT

A multi-energy source (MES) method featuring a high-power scanning laser (SL) was used to achieve independent control of layer width and height in a wire-based directed energy deposition (w-DED) process. In the MES system, a plasma transferred arc (PTA) was employed to create an initial melt pool and melt the wire, and a SL was used to reshape the melt pool and precisely control the bead width. The distance between the SL and the PTA and different laser scanning strategies were investigated. Images of the melt pool with varying scanning widths were captured. A bead shape control strategy was demonstrated by using the wire feed speed to control layer height and the laser scanning width to control the layer width independent of each other. The advancing speed was adjusted in proportion to the scanning width to keep the same specific process energy of the SL. The experimental results demonstrated that the MES approach provides independent control of layer width and height. Some single-pass walls were built using the MES to show that MES can be used for w-DED additive manufacturing.

1. Introduction

Wire-based directed energy deposition (w-DED) additive manufacturing (AM) has developed rapidly due to advantages such as short lead times compared to forgings, low material waste compared to machining, and high design flexibility (Ding et al., 2015). W-DED AM processes have much higher deposition rates and lower material waste than powder-based methods, leading to the potential to produce large-scale and near-net-shape metallic components in many industry sectors, including aerospace, aviation, and power generation (DeRoy et al., 2018). Conventional single energy source w-DED AM that uses the same energy source such as metal inert gas (MIG), tungsten inert gas (TIG) and plasma transferred arc (PTA) to melt the wire and substrate at the same time has been widely used. Bead shape control of the single energy source w-DED AM has been investigated by many researchers. Dinovitzer et al. (2019) discussed the effects of process parameters in a TIG-based AM process using Hastelloy X alloy (Haynes International) welding wire and 304 stainless-steel plates as the substrate. They used the Taguchi and the Analysis of Variance (ANOVA) to determine the effects of travel speed, wire feed speed, current, and argon flow rate on the responses including layer shape and size, bead roughness, oxidation levels, melt through depth, and the microstructure. They found that the

layer width decreased whilst the layer height increased with an increase of wire feed speed. Travel speed had a significant effect on layer width but a minor effect on layer height. Layer width increased with increasing current. Martina et al. (2012) investigated the PTA deposition of titanium for a wide range of parameters. An ANOVA was performed to determine the relationship between the bead geometry and the parameters. Response models for the total wall width, effective wall width and layer height were established. Bead shape control within a limited range of forms was achieved. However, layer width and height, bead shape accuracy and deposition rate were highly correlated.

In a w-DED AM process, material per unit length, which determines the cross-sectional area of the bead, is controlled by the wire feed speed to travel speed ratio, while deposition rate is controlled by the wire feed speed for a given constant wire diameter. However, while maintaining a constant wire feed speed to travel speed ratio, the effective wall width decreases with an increasing wire feed speed, resulting in a narrower and taller wall (Sequeira Almeida and Williams, 2010). Consequently, the deposition rate is restricted by the bead cross-section. Another limitation is that the thermal conditions during the deposition process vary with the bead shape. A higher wire feed speed to travel speed ratio can achieve a larger cross-sectional area, but it will increase heat input of the process for MIG based processes (Yehorov et al., 2019). Microstructure

^{*} Corresponding author.

E-mail address: guangyu.chen@cranfield.ac.uk (G. Chen).

and mechanical properties are therefore affected due to the high heat input. For conventional electric arc single energy source processes, the energy distribution and dimension of an electric arc are not controllable. Layer width and height will be affected simultaneously when the parameters are changed. Bead shape can only be optimised by adjusting parameters such as current, arc length, wire feed speed, etc.

A laser beam is also used in single energy source deposition. Schulz et al. (2019) studied the impacts of the wire configuration, wire feed speed, laser spot size and laser power on the bead geometry and process stability. They found that it is essential to keep the laser spot size s large as the estimated melt pool and, therefore, the bead size. Process maps were analysed for the control of the bead width. Abioye et al. (2013) also developed a process map for the fibre laser deposition of Inconel 625 wire to predict the process characteristics and bead geometry. They reported that energy per unit length and wire deposition volume per unit length have significant effects on both the deposition process characteristics and the bead geometrical characteristics. Mok et al. (2008) studied the bead shape of the deposition using a bar-shaped stationary laser beam. Independent control of the layer height and layer width was achieved in specific ranges by adjusting wire feed speed and laser power correspondingly. However, due to the limitation of the laser beam shape, the bead shape range was restricted. Because the power density profile of the laser beam can be independently controlled without changing the dimension, compared to the arc-based process, layer height can be controlled with greater independence. However, the layer width control was limited by the laser beam dimension.

Multi-energy source (MES) is a concept that combines more than one energy source to overcome the limitation of the conventional single energy source process. Several studies have been focused on bead shape control using MES. Qian et al. (2008) developed a PTA-laser hybrid technology to improve the accuracy and metallurgical performance of the deposition. Results showed that the laser beam stabilised the PTA, improved the bead surface quality, and diminished the porosity. Liang et al. (2017) proposed a TIG- cold metal transfer (CMT) hybrid welding process. In their study, two energy sources were separated without interaction. They concluded that TIG improved the wettability of the melt pool. Bead shape was achieved with decreased contact angle better dilution. Yang et al. (2017) compared the parts built by a regular gas metal arc (GMA) and double-electrode GMA (DE-GMAW). The results showed that the dimensions of the melt pool were reduced by about 30% by the bypass arc of the DE-GMAW. A lower heat input was achieved while maintaining the same deposition rate. Zhang et al. (2006) introduced a hybrid plasma-laser deposition manufacturing (PLDM) for a thick coating. A laser beam was employed to interact with the PTA as an additional energy source. The PTA was more concentrated with a smaller diameter and deeper penetration and was easier to be ignited. Mechanical properties of the coated layer were improved. Liu et al. (2020) studied the improvement of the addition laser energy source in a laser-arc hybrid Al alloy thin-wall AM process. The microstructure of the hybrid AM process showed a reduced heat-affected zone with refinement grains. Sr element was found more uniform in hybrid additive manufactured samples with better mechanical performance. Li et al. (2020) investigated the single bead and intersections deposited by a laser-CMT hybrid AM method. A surface quality metric for intersection builds was proposed based on the volume deviation between the ideal CAD model and the scanned shape of the part to optimise a set of parameters. The validation experiment showed that the optimised parameters significantly improved the geometry quality of the bead. Previous research was mostly focused on improving the process stability and bead geometry. Wang et al. (2021a) introduced a laser-PTA hybrid additive manufacturing for the deposition of Ti-6Al-4V. An MES that consisted of a PTA and two stationary laser beams was introduced. Two laser beams were placed at the sides of the melt pool to provide more energy on the edges. This method increased the deposition rate with a higher process tolerance. In addition, the bead shape control in this process was systematically studied by manipulating different process

parameters (Wang et al., 2021b). They also stated that with the PTA to melt the wire and the laser to control the melt pool, independent control of bead shape and deposition rate can be achieved. However, this work did not further study the independent control of the layer height and the layer width.

In previous studies, scanning lasers (SL) were mainly used in welding applications to improve gap tolerance and weld quality. For example, Hao et al. (2015) studied the effects of oscillating beam parameters on weld morphologies. The results showed that the weld cross-section becomes more homogeneous with the increase of oscillating frequency because of the forming of a quasi-steady melt pool. Some other research has focused on the SL-arc hybrid process. For example, Cai et al. (2017) used an SL-metal active gas (MAG) hybrid welding method for the bead on plate welding of high-strength steel. Weld porosity defects were suppressed due to the stirring effect of the SL to the melt pool. To the best knowledge of the authors, no systematic study about bead shape control using the SL-arc hybrid process has been reported.

In this study, an SL-PTA MES system was introduced that combines the advantages of an SL and a PTA. The SL can be used as a quasi-steady-state energy source to reshape the melt pool and precisely control layer width. Unlike other conventional energy sources, the shape of a SL can be changed by adjusting the scanning pattern, and the energy distribution of the SL can be designed by using different scanning speeds in different regions if the SL reaches a quasi-steady state. A PTA can be employed in front of the SL as an efficient energy source to create an initial melt pool and melt the wire. The absorption efficiency of a PTA is higher than that of a laser beam and is, therefore, a better option to initial the melt pool. The scanning device that was used in this study was a galvanometer-based scanner (GS) (Montagu, 2018). The GS is one of the most used scanning devices for both one-dimensional and two-dimensional scanning and is suitable for an extensive range of applications.

The primary target for this study is to demonstrate the independent control of the layer height and width in the w-DED AM process, which are normally linked directly together. The purpose for this is to:

1. Enable continuous variation of the deposited bead shape. Normally in the conventional w-DED AM, the layer height would be changed if the layer width changes, which could be a major issue for substantial structures deposition. Similarly, the layer width would change when the layer height needs to be adjusted, which might lead to defects.
2. Enable the deposited bead shape variation without changing its thermal condition. Normally for a given width in the conventional w-DED AM, a layer height can be varied, which would change the thermal conditions and, therefore, the microstructure in some materials.
3. Enable higher build rates can be achieved through depositing very wide beads.

In the SL-PTA MES system, a variety of parameters can be adjusted to obtain a particular combination of a layer height and a layer width. Therefore, a bead shape control strategy was designed to control the bead shape systematically. In this strategy, layer width is controlled by SL scanning width, and layer height is controlled by wire feed speed. Correspondingly, advancing speed is adjusted according to scanning width to keep the same specific process energy. Some single-pass walls were built to demonstrate that the SL-PTA MES system can be utilised in the w-DED AM process.

2. Experimental procedure

2.1. Setup

The configuration of the SL-PTA MES setup is shown in Fig. 1, and Fig. 2 illustrates the position of the torch, laser and wire. A PWP Viper MC plasma torch was placed in front of a SL with an angle (α_2) of 65° to

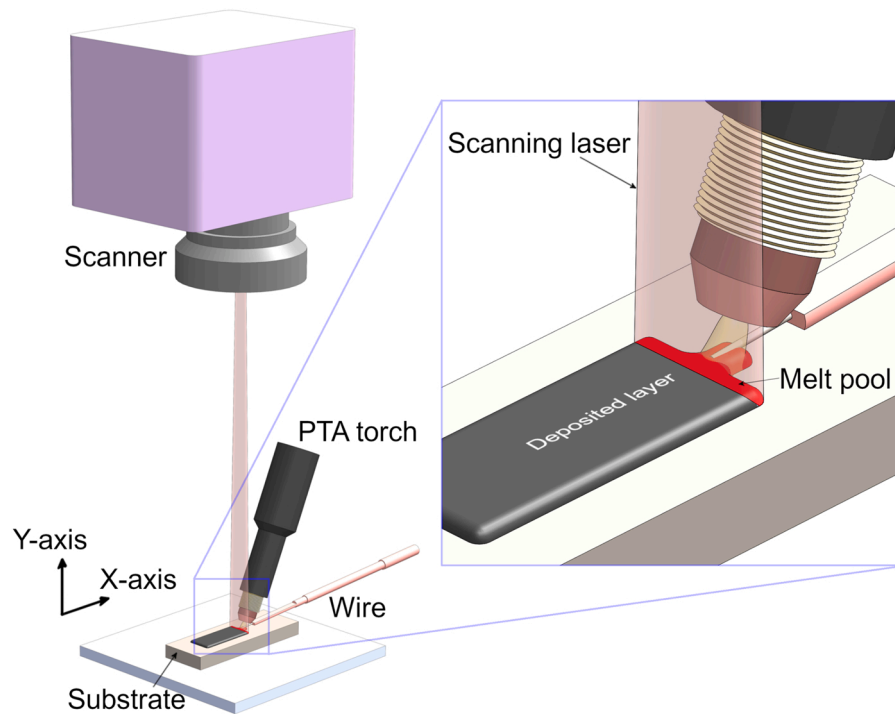


Fig. 1. Configuration of the SL-PTA MES.

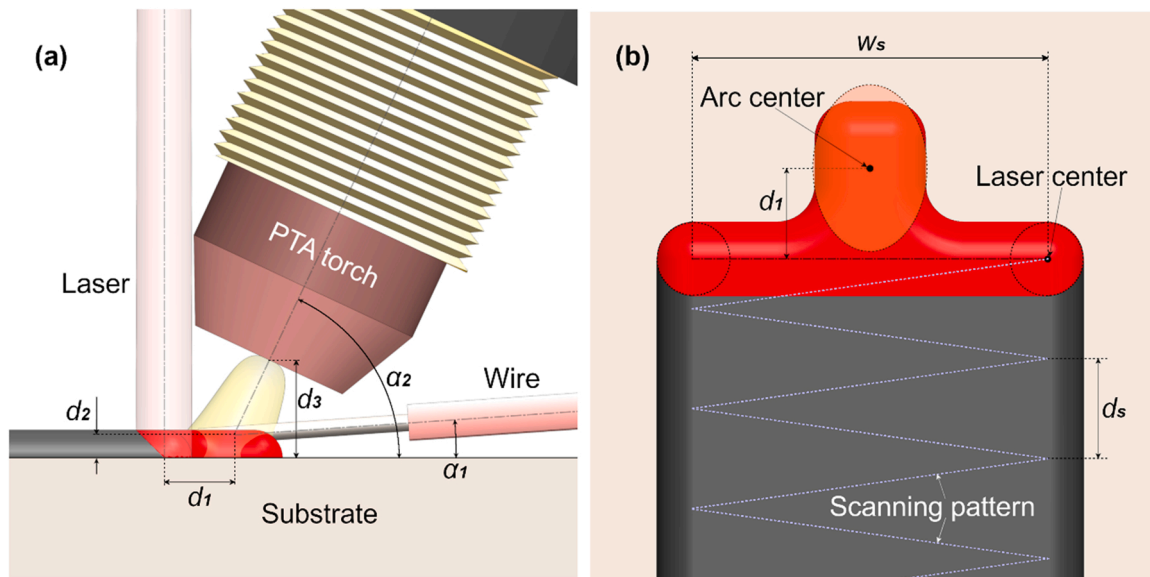


Fig. 2. Position of the torch, laser and wire: (a) side view and (b) top view.

the horizontal. The PTA was generated by an EWM Tetrix 552 power supply. A Migatronc KT4 wire feeder was employed in the front of the PTA with an angle (α_1) of 4° to the horizontal to feed the wire from the front. A JK 3000FL continuous wave fibre laser (wavelength $1.08 \mu\text{m}$) was applied to generate the laser energy. The laser beam was directed by a Raylase SUPERSCAN-III GS scanning head and projected onto the substrate vertically, and was defocused to give a 4 mm beam diameter. A laser beam size of 4 mm ensured that the laser was in conduction mode during the process even with higher laser powers. The distance between the SL and the PTA (d_1) was measured from the intersection of the PTA torch centre line and the substrate surface to the centre of the laser. The distance between the PTA torch to the substrate (d_3) was measured from the centre of the copper nozzle to the substrate in the vertical direction.

The scanning width (w_s) was measured by the crosswise moving distance of the laser beam centre. Parameters of the configuration are listed in Table 1. Fig. 3 illustrates the setup of the MES system. Two Aerotech CNC actuators were used to move the substrate in the vertical (Y-axis) direction and the horizontal (X-axis) direction, while the MES heat

Table 1
Parameters for the MES configuration.

SL-PTA distance (d_1) / (mm)	6.5
Wire-substrate distance (d_2)/(mm)	1
Torch-substrate distance (d_3)/(mm)	7
Feeding wire angle (α_1) / (degree)	4
Torch angle (α_2) / (degree)	65

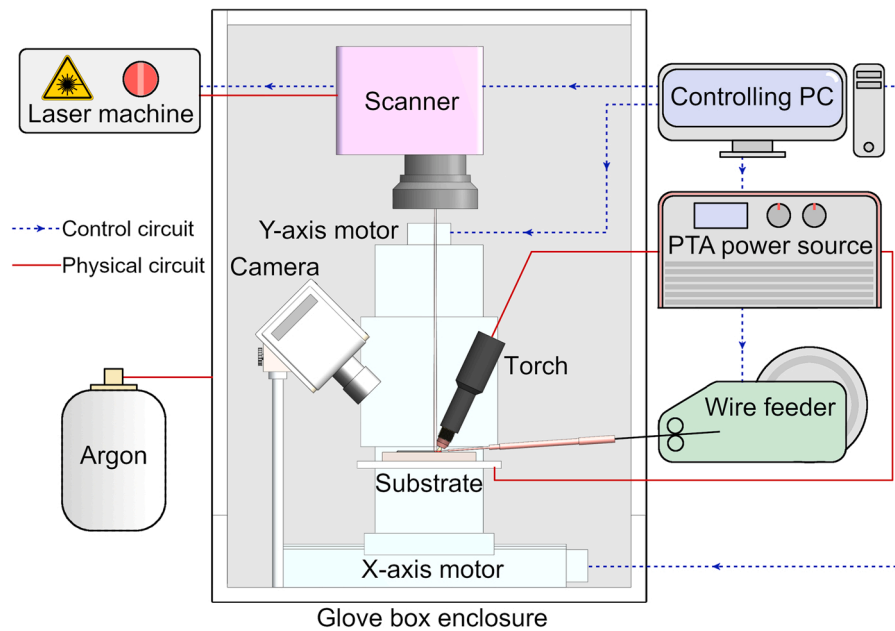


Fig. 3. Diagram of the MES system setup.

source remained stationary. The movement of the actuators, the trigger of the wire feeder, and the laser scanner were controlled and synchronised by a A3200 machine controller installed on a personal computer (PC). The PTA power source and laser machine were triggered by the wire feeder can scanner, respectively. A Phantom MIRO-4 M high-speed camera was set up behind the MES heat source to capture the dynamics of the melt pool with a recording frame rate of 6000 frames per second. The whole setup was enclosed in a glove box filled with pure argon. The oxygen level was measured by a GS SENSOREINHEIT oxygen monitor and was kept below 500 ppm. S275 mild steel plates with a dimension of 200 mm × 45 mm × 12.5 mm were used as substrates, and 1.2 mm diameter LNM 20 steel wire was used as feedstock. The composition of the feedstock is listed in Table 2. The ceramic nozzle was removed from the PTA torch as shielding was provided by the inert argon atmosphere. The fixed parameters for the SL and the PTA are listed in Tables 1, 3 and 4. The parameter selection for the PTA was based on the previous work on the w-DED AM process using PTA, as reported by Wang et al. (2021c). A low current intensity of 140 A was applied to ensure a stable process. Laser power was set accordingly with an energy amount similar to the PTA.

2.2. Preliminary experiment

2.2.1. SL energy distribution

The scanning pattern was edited and controlled by the SCAPS SAMLight scanner application software installed on the controlling PC. In this study, the GS oscillated the laser beam in a back-and-forth pattern transverse to the advancing direction, and the substrate was moved in the advancing direction. By combining these two movements, a saw wave scanning pattern was achieved on the substrate, as shown in Fig. 2b. The scanning frequency F_s was determined by the scanning speed v_s and the scanning width w_s of the SL, as shown in Eq. 1. The increment of the scanning pattern d_s is determined by the scanning frequency F_s and the advancing speed v_a , as shown in Eq. 2. In this study,

Table 2
Chemical composition (wt%) of the feedstock.

C	Mn	Si	Cr	Mo	Fe
0.08	0.9	0.6	2.5	1.0	Balance

Table 3

Parameters for the SL.

Power / (W)	2700
Wavelength / (μm)	1.08
Focal length / (mm)	250
Distance between the laser head and the measuring plane / (mm)	305

Table 4

Parameters for the PTA.

Current / (A)	140
Voltage / (V)	21.5
Orifice size / (mm)	3.9
Electrode diameter / (mm)	4
Electrode Tip Angle / (degree)	40
Electrode Tip Set-back / (mm)	2.4

the scanning speed v_s was above 2000 mm/s. As a result, the scanning frequency F_s was above 100 Hz and the d_s was less than 0.008 mm, which is much smaller than the laser beam size. Therefore, a slight change in the scanning frequency when changing the scanning width would not affect the forming of a quasi-steady-state melt pool.

$$F_s = \frac{v_s}{2w_s} \quad (1)$$

$$d_s = \frac{v_a}{F_s} \quad (2)$$

In a laser process, the period that a certain point is irradiated can be defined as the interaction time. The energy delivered to this particular point denoted as the specific point energy E_{sp} , is proportional to the product of power density q_p , interaction time t_i and the area of the specific point A_{sp} , which also corresponds to the product of the absorbed laser power P_l and interaction time t_i . For an SL process, a particular point might interact with the laser beam more than once. Fig. 4 illustrates the relative movement of a specific point on the substrate that passes across the laser beam section during scanning. The number of interactions n_i is defined as how many times the laser beam passes the specific point. The number of interactions n_i is determined by the laser beam size D_L and the increment of the scanning pattern d_s , as shown in Eq. 3, and the total specific point energy can be calculated by Eq. 4:

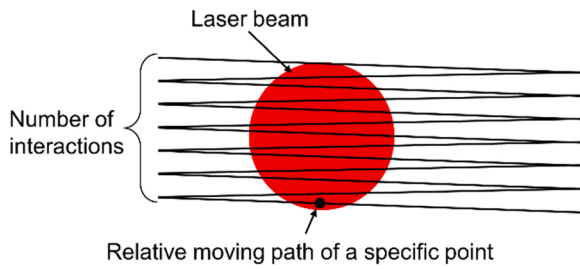


Fig. 4. The number of interactions during scanning.

$$n_i = \frac{D_L}{d_s} \quad (3)$$

$$E_{sp} = \sum_1^{n_i} q_p A_{sp} t_i = \sum_1^{n_i} P_L t_i \quad (4)$$

In the SL process, with the same interaction number, a slower scanning speed gives a longer interaction time and, therefore, higher specific point energy. With the assumption of the SL thermal field reaching the quasi-steady-state, different SL energy distributions could be achieved by changing the scanning speed during scanning, that is, changing the interaction time. Two energy distribution profiles were compared, as shown in Fig. 5, and their effect on the melt pool wettability was studied. The energy of the PTA was mainly concentrated at the centre of the MES. Correspondingly, the energy of the SL at the centre can be lowered to achieve a more uniform energy density along the bead width direction. The GS can provide a maximum linear speed of 16500 mm/s. This maximum speed was used at the centre region of the SL to deliver the lowest energy. A reference scanning speed of 4125 mm/s was applied for two side areas. In the scanning pattern of profile 1, the SL scanning laser speed was kept constant at 4125 mm/s on the side regions. Whereas in profile 2, the scanning speed decelerated to 25% (1030 mm/s) at the edge. Fig. 5a diagrams the scanning speed along the scanning path of these two profiles. The energy distribution density profiles can be calculated as shown in Fig. 5b.

2.2.2. SL-PTA distance

The effect of the SL-PTA distance d_1 on the melt pool stability was investigated. Three different SL-PTA distances, 10.5 mm, 6.5 mm, 2.5 mm, were set. Fig. 6 illustrates the relative position of the SL and PTA melt pools with different SL-PTA distances.

2.3. Shape control strategy

In the MES system, parameters that can be adjusted include SL power, PTA power, wire feed speed, SL scanning width, advancing speed, etc. More than one combination of the process parameters can be set to achieve a particular set of layer width and layer height. Therefore,

a bead shape control strategy was needed to control the width and the height of the layer systematically. The deposition rate R of a process can be expressed by how much wire is fed per unit time:

$$R = \frac{\pi d^2}{4} v_w \rho \quad (5)$$

where d is the wire diameter, v_w is the wire feed speed, ρ is the density of the wire. Another approach of calculating the deposition rate is that if the cross-section of the bead is approximated as a rectangle, its area can be calculated from the layer width and the layer height. Correspondingly, the deposition rate can also be calculated by Eq. 6:

$$R = h v_a \rho \quad (6)$$

where w is the layer width, h is the layer height and v_a is the advancing speed of the MES. Eq. 7 was obtained by combining Eqs. 5 and 6:

$$\rho \frac{\pi d^2}{4} v_w = h v_a \rho \quad (7)$$

Eq. 7 can further be transformed into Eq. 8:

$$\frac{v_w}{h} = \frac{4}{\pi d^2} w v_a \quad (8)$$

In this study, the layer width was determined primarily by the scanning width. The laser beam power P_L , the wire feed speed v_w and the scanning speed v_s were kept constant. If the advancing speed v_a stays the same, a larger scanning width w_s would lead to a lower scanning frequency F_s and a fewer number of interactions n_i , and consequently a lower specific point energy E_{sp} according to Eqs. 2, 3 and 4. The advancing speed needs to be lowered to maintain the same number of interactions to keep a same specific point energy for a larger scanning width. Therefore, in Eq. 8, $w v_a$ is kept constant to maintain the same specific point energy. Correspondingly, $\frac{v_w}{h}$ is kept constant. Therefore, in this strategy, the layer width was determined by the scanning width, the advancing speed was determined by the scanning width, and the layer height was determined by the wire feed speed.

A bead shape control experiment was conducted to evaluate the bead shape control strategy. 20 beads with 5 different layer heights and 4 different layer widths were tested to prove the independence of the width and the height controls of the bead shape. Table 5 lists the scanning widths and the corresponding advancing speeds for different layer widths, and Table 6 lists the wire feed speeds for different layer heights. A set of PTA-only experiments were also tested with all four advancing speeds using a constant wire feed speed of 6 mm/s without the SL reshaping to compare with the MES before the bead shape control experiments.

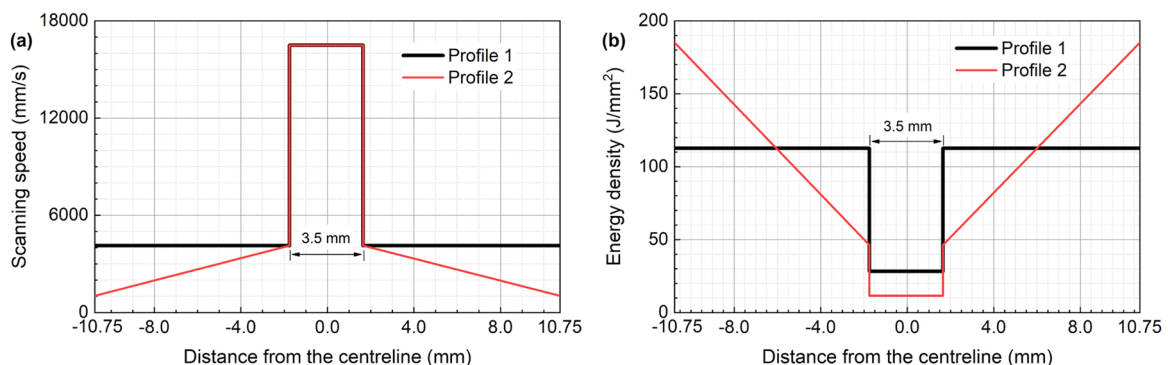


Fig. 5. Energy profiles for melt pool study: (a) scanning speed along the scanning path and (b) equivalent energy distribution along the scanning path.

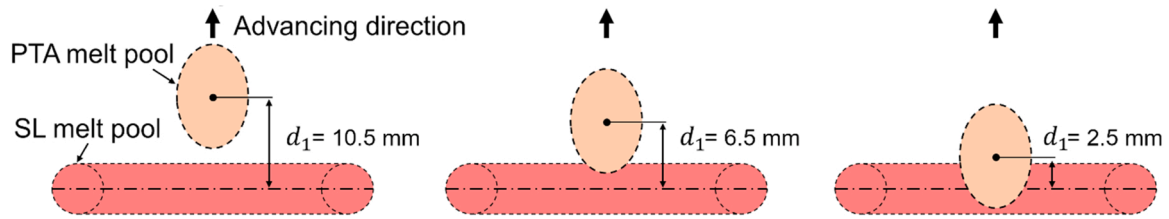


Fig. 6. Diagrams of three different SL-PTA distances.

Table 5
Varied scanning widths and the corresponding advancing speeds.

Scanning width / (mm)	Advancing speed / (mm/s)
16.5	0.8
20.0	0.67
23.0	0.57
26.5	0.5

Table 6
Varied wire feed speeds.

Wire feed speed / (mm/s)
6
12
18
24
30

2.4. MES wall building

2.4.1. MES wall building with different layer heights

After the bead shape control study, three wall building cases were carried out using three different layer heights. The parameters are listed in Table 7. When initialising the MES melt pool, the SL started with a smaller scanning width of 10 mm and increased to the targeted scanning width by steps.

2.4.2. MES wall building with different SL energy distributions

Two different SL energy distributions were used to construct two walls to study the influence of SL energy distribution on the narrowing of the width during MES multi-layer deposition. The larger scanning width is 26.5 mm to observe the width changes better. The parameter sets that were used are listed in Table 8. The scanning speed arrangements and SL energy distribution profiles are diagrammed in Fig. 7. The scanning speed decelerated at the edges to respectively 25% (1030 mm/s) in Profile 3 and 10% (413 mm/s) in Profile 4.

2.4.3. Microstructure and microhardness

Microstructure and microhardness were analysed on the Wall 1 cross-section to analyse the microstructure isotropic of the MES process. Images at six positions, as indicated in Fig. 8, were captured using an optical microscope (OM). The Vickers hardness testing was done at room temperature along two lines on the cross-section, which are the vertical centre line and the horizontal line at the half height, as shown in Fig. 8. A 200 g load was applied for 15 s at a spacing of 1 mm.

Table 7
Parameters for wall building with different layer heights.

	Wall1	Wall 2	Wall 3
Scanning width w_s / (mm)	20	20	20
Advancing speed v_a / (mm/s)	0.67	0.67	0.67
Wire feed speed v_w / (mm/s)	6	12	24
Number of layers	26	13	9

Table 8
Parameters for wall building with different SL energy profiles.

	Wall4	Wall 5
Scanning width w_s / (mm)	26.5	26.5
Advancing speed v_a / (mm/s)	0.5	0.5
Wire feed speed v_w / (mm/s)	12	12
Number of layers	13	13
SL energy profile	Profile 3	Profile 4

3. Results and discussion

3.1. Preliminary experiment

3.1.1. SL-PTA distance experiment

Fig. 9 shows the MES process results using different SL-PTA distances (d_1). From the front ends of the beads, the melt pools can be seen slightly changed with the SL-PTA distance. With a faraway SL-PTA distance of 10.5 mm, the PTA and the SL melt pools did not merge (Fig. 9a). A gap of approximately 2 mm is shown between the two melt pools. When moving the PTA closer to the SL, the end of the PTA melt pool overlaid with the SL melt pool, and a hybrid melt pool was formed with the shape gradually transformed to a slightly wedged shape (Fig. 9b). By narrowing the SL-PTA distance to 2.5 mm, most of the PTA melt pool overlaid with the SL melt pool, and a triangle shape hybrid melt pool was formed (Fig. 9c). Fig. 10 shows the cross-section images of these three beads. Incomplete fusion can be found in these cross-section images with SL-PTA distances of 10.5 mm and 2.5 mm (Figs. 10a and c), whereas no defect is found with an SL-PTA distance of 6.5 mm (Fig. 10b). That is to say that even though the processes were continuous and stable, a too close or too far away distance between the scanning laser and the PTA will cause defects. When the PTA melt pool and the SL melt pools were separated, the cause of the incomplete fusion could be that the substrate at the middle of the SL was already solidified and could not be remelted by the SL. When having a too close SL-PTA distance, the possible reason for the defect could be that the SL scanned above the PTA and was affected by the PTA plasma body, which led to an unstable melt pool. Based on the results, an optimised distance of 6.5 mm was selected for the MES experiments.

3.1.2. SL energy distribution

Fig. 11 shows the melt pool images with different SL energy distributions shown in Fig. 5. Although the same scanning width was used for both profiles, the bead width of the one using Profile 1 is significantly narrower than the one using Profile 2. When using Profile 1 with evenly distributed energy at side regions (Fig. 11a), the melted metal failed to be spread to the two ends of the scanning width of 21.5 mm, and a layer width of 17.6 mm was formed. When using Profile 2, more energy was provided at the edges, and the melt pool was spread across the whole scanning width with a layer width of 22 mm (Fig. 11b). In the bead cross-section images, the penetration with the Profile 1 SL (Fig. 12a) at the middle is deeper than the Profile 2 SL (Fig. 12b). This indicates that with Profile 1, more energy was concentrated at the centre, while the edges were not melted sufficiently due to the lack of energy. Wettability at the edges was therefore restricted. The total energy of these two

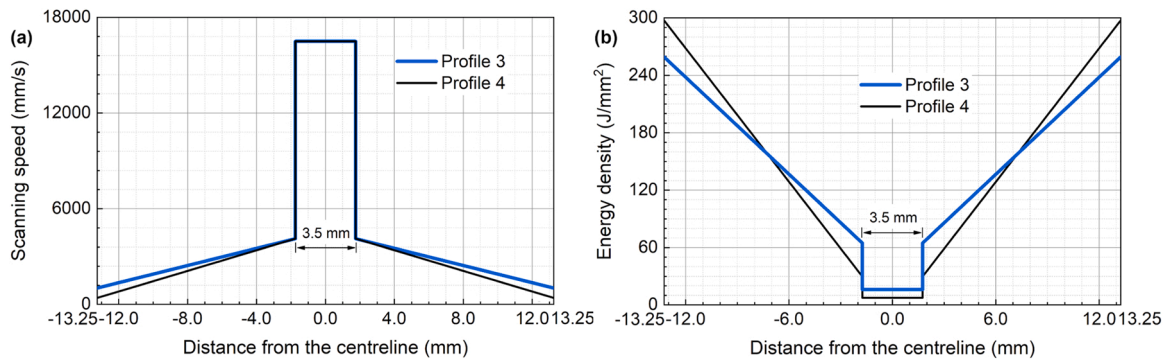


Fig. 7. Energy profiles for wall width study: (a) scanning speed along the scanning path and (b) equivalent energy distribution along the scanning path.

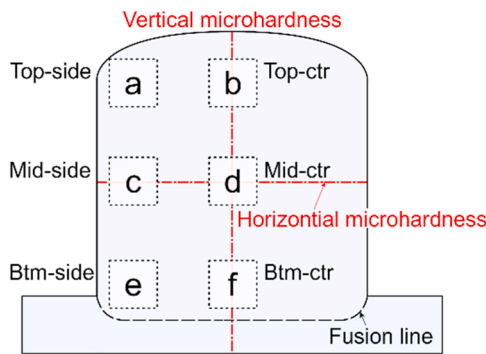


Fig. 8. Microhardness along two directions, and positions of the OM images: (a) top-side, (b) top-centre, (c) middle-side, (d) middle-centre, (e) bottom-side, and (f) bottom-centre.

profiles is the same, and only the energy distribution was adjusted. The temperature field of the PTA is higher at the centre and gradually decreases on two sides. As a result, the SL energy that was needed to heat the material and generate the melt pool was lower at the centre and higher at the sides. These results show that a profiled SL can improve the broadening of the melt pool and spread across the whole scanning path.

3.2. Bead shape control experiment

Fig. 13a shows the bead geometry of the PTA-only process. The even and continuous ‘stack of dimes’ bead surface indicates that the process was stable, and the droplet transfer was smooth and even. Fig. 13b shows the SL reshaped bead surfaces. The surface roughness is fine with a smooth texture, free of any splatter. The edges of the bead are straighter compared to the PTA-only process. The cross-section of the PTA-only bead in Fig. 14a shows that the fusion between the added material and the substrate was sufficient, indicating that the substrate

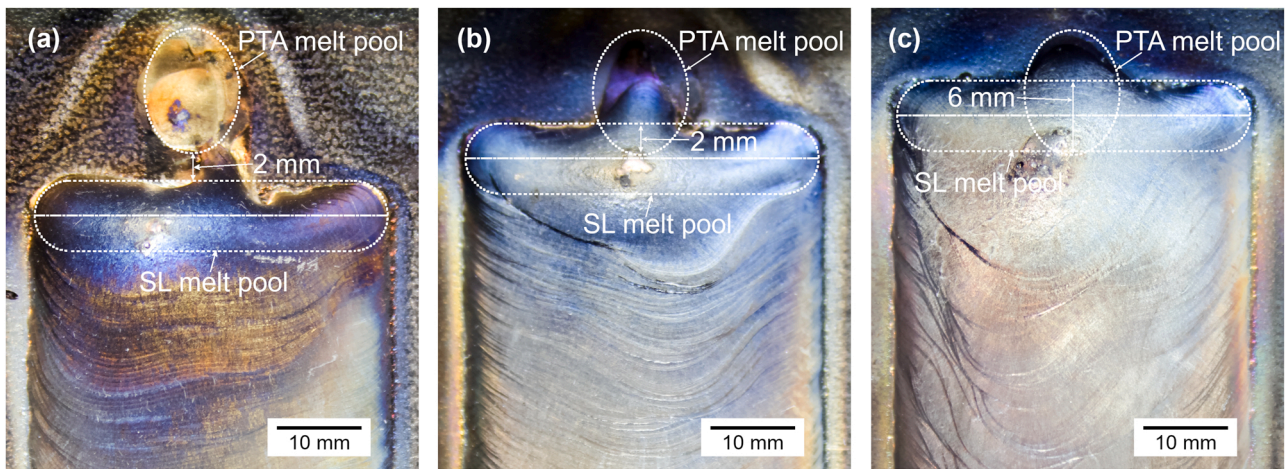


Fig. 9. SL-PTA distance experiment results – melt pool images: (a) $d_1 = 10.5$ mm, (b) $d_1 = 6.5$ mm, and (c) $d_1 = 2.5$ mm.

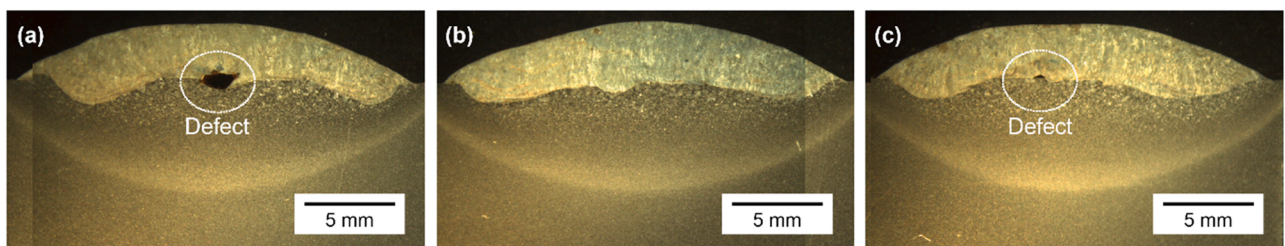


Fig. 10. SL-PTA distance experiment results - cross-sections: (a) $d_1 = 10.5$ mm, (b) $d_1 = 6.5$ mm, and (c) $d_1 = 2.5$ mm.

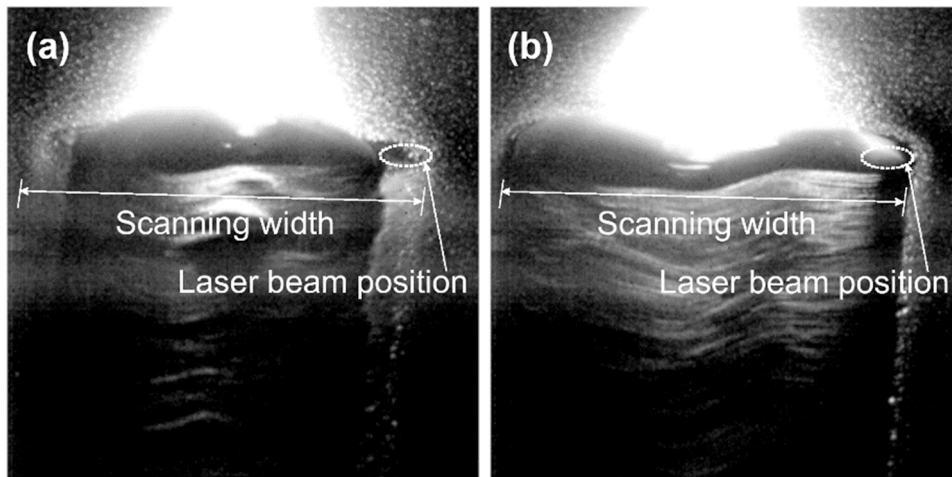


Fig. 11. SL energy distribution experiment results –melt pool images: (a) with Profile 1 SL and (b) with Profile 2 SL.

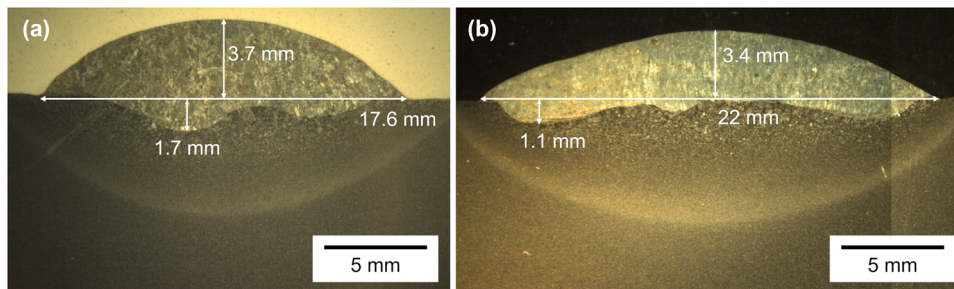


Fig. 12. SL energy distribution experiment results –cross-sections: (a) with Profile 1 SL and (b) with Profile 2 SL.

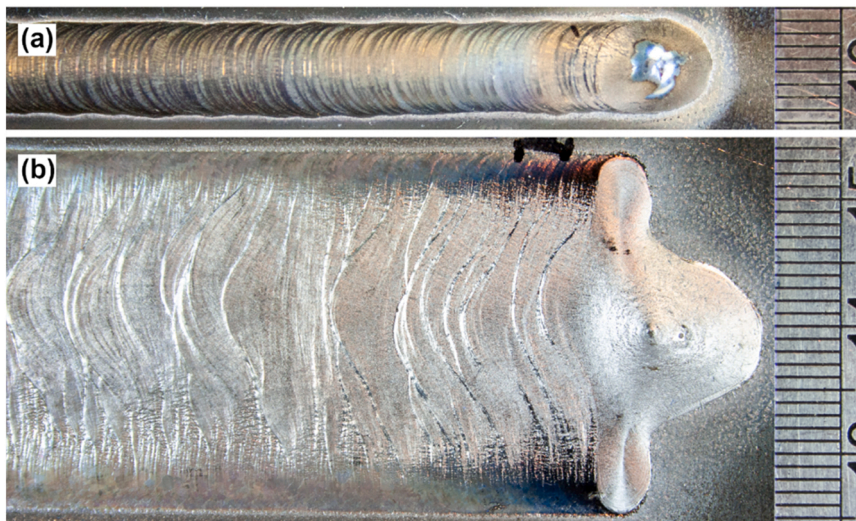


Fig. 13. Comparison of the bead surface geometries: (a) PTA-only ($v_a=0.5$ mm/s) and (b) SL-reshaped ($v_a=0.8$ mm/s, $w_s=26.5$ mm).

can be sufficiently melted by the PTA. Fig. 14b further shows the cross-section shape of the corresponding SL reshaped bead. The fusion between the added material and the substrate was sufficient without defect. Compared to the PTA-only process, the layer height was significantly lowered, and the layer width was increased, forming a rather flat cross-section shape. The penetration depth, however, was not dramatically affected. This means that the SL only reshaped the melt pool but did not increase the penetration of the PTA initiated melt pool. Fig. 15 shows the images of the SL reshaped melt pool with changing scanning

width. It can be observed that the ellipse-shaped PTA melt pool was spread and reshaped to a continuous wide-brimmed hat shape, with an ellipse-shaped front and bar-shaped back. The reshaped melt pools were stable with no scattering and were maintained in quasi-steady shapes with all tested scanning widths. No interference was observed between the PTA and the SL. Fig. 16 shows the correlation between the layer width and height and the advancing speed. The layer height of the PTA-only bead decreased from 3.2 mm to 2.4 mm, and the layer width decreased from 7.6 mm to 6.7 mm when the advancing speed was

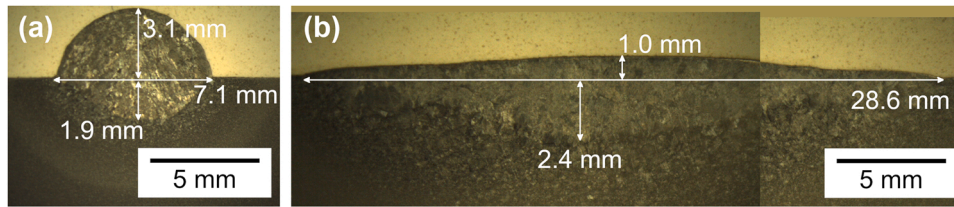


Fig. 14. Comparison of the bead cross-sections: (a) PTA-only ($v_a=0.5$ mm/s) and (b) SL-reshaped ($v_a=0.5$ mm/s, $w_s=26.5$ mm).

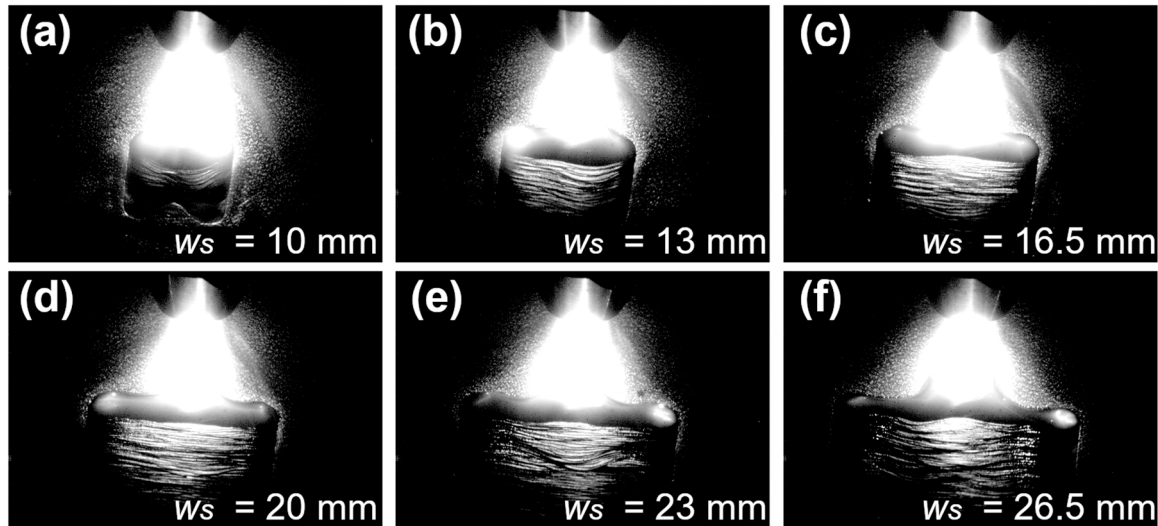


Fig. 15. Images of the SL reshaped melt pool with different scanning widths: (a) $w_s=10$ mm, (b), $w_s=13$ mm, (c) $w_s=16.5$ mm, (d) $w_s=20$ mm, (e) $w_s=23$ mm, and (f) $w_s=26.5$ mm.

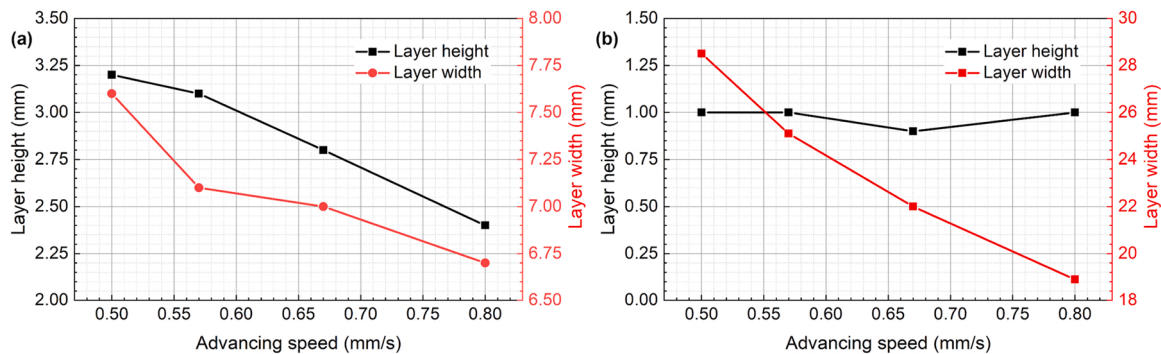


Fig. 16. Correlation of layer height and width vs advancing speed: (a) PTA-only and (b) SL-reshaped.

increased from 0.5 mm/s to 0.8 mm/s. After reshaping by the SL, the layer height was kept to a more constant level between 0.9 mm and 1.0 mm, and the layer width decreased from 28.6 mm to 18.9 mm when increasing the advancing speed.

Ideally, a flat layer shape with round edges and small contact angles is required for w-DED AM. In this study, the SL-reshaped section shape is flatter, and the contact angle is relatively smaller, which is closer to the ideal layer shape.

Fig. 17 presents a scatter chart that shows the layer widths and layer heights of all 20 beads and their cross-section images. We can see from the scatter chart that those points are evenly distributed within a rectangular area in the diagram shown in Fig. 17a. All the bead sections in Fig. 17b show good fusion between the fed material and the substrate. That means that the independence of the layer width and the layer height, with any combination within the rectangular chart is achievable.

Fig. 18a shows the correlation between the scanning width and the

layer width. Despite using different wire feed speeds, the layer width is shown as a highly linear function of the scanning width. This further shows that the layer width was only determined by the scanning width. The layer widths are slightly wider than the scanning width because the laser beam dimension needed to be taken into account when the melt pool was formed.

Fig. 18b shows the correlation between the wire feed speed and the layer height. Similar to the layer width and the scanning width, the layer height is shown as a highly linear function of the wire feed speed. That shows that the bead shape strategy of using the wire feed speed to control the layer height is applicable. However, as the assumption of a rectangular bead shape was made, which the actual bead shape is not strictly followed, the correlation between the layer height and the wire feed speed slightly deviates.

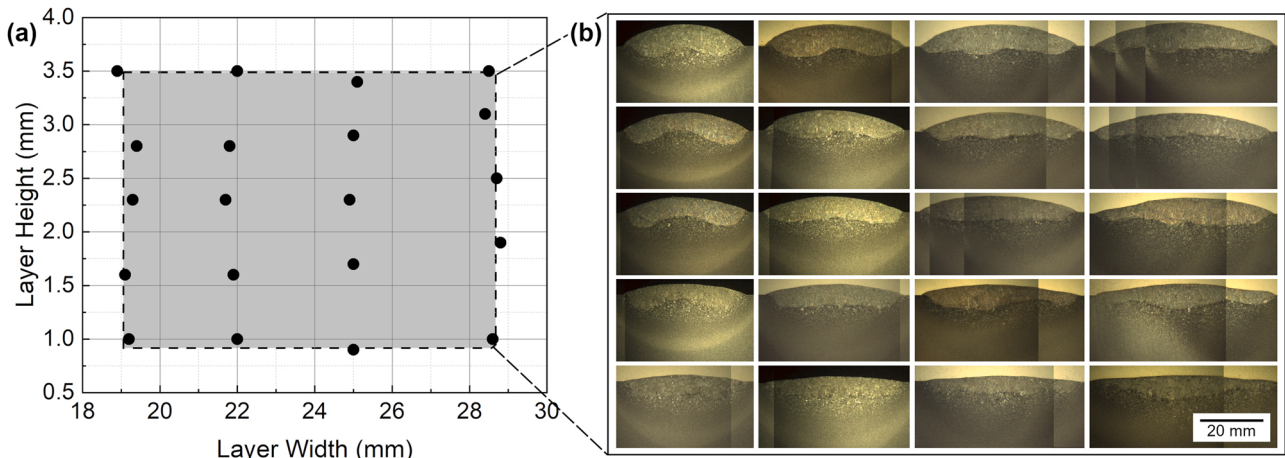


Fig. 17. (a) Scatter chart of layer height vs layer width correlation and (b) cross-section images.

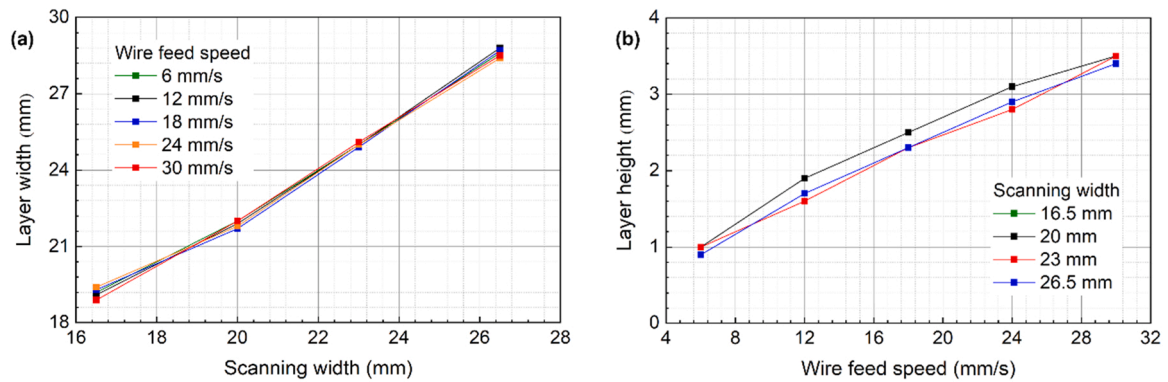


Fig. 18. (a) Diagram of layer width with vary scanning width at different wire feed speeds and (b) diagram of layer height with vary wire feed speed at different scanning widths.

3.3. MES wall building

Fig. 19 shows the geometry of the MES deposited wall from both the top and the side. A smooth surface finish quality is presented. Fig. 20 shows the cross-sections with different layer heights but constant width determined by the scanning width. Wall 1 with thinner layers has a straight outline of the side surface (Fig. 20a). Walls 2 and 3 were built with increased layer heights of 1.3 mm and 2.3 mm. The bead shape became less stable because more material was added to the melt pool,

and the side surface quality slight dropped (Figs. 20b and 20c). Slight collapse can be observed at the side of Wall 3 (Fig. 20c).

The width of all three walls narrowed from the bottom to the top. Another two walls were built with Profile 3 and 4 SL energy distributions to analyse the possible reason for this phenomenon and a larger scanning width for a better observation of the width changing. Fig. 21 shows the cross-sections of the two walls. With more energy arranged at the edges, the width difference between the bottom and the top was reduced from 5.8 mm to 3.6 mm, with a thinner layer height and wider wall

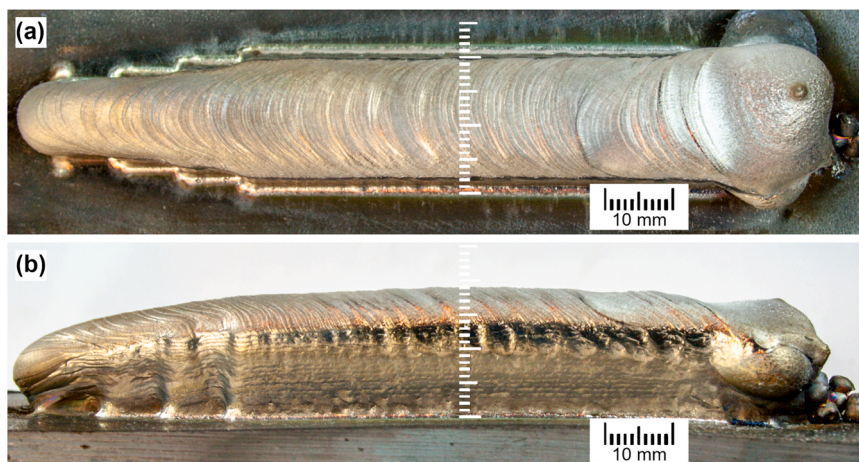


Fig. 19. SL-PTA MES built wall ($w_s = 20$ mm, $v_w = 6$ mm/s): (a) top view and (b) side view.

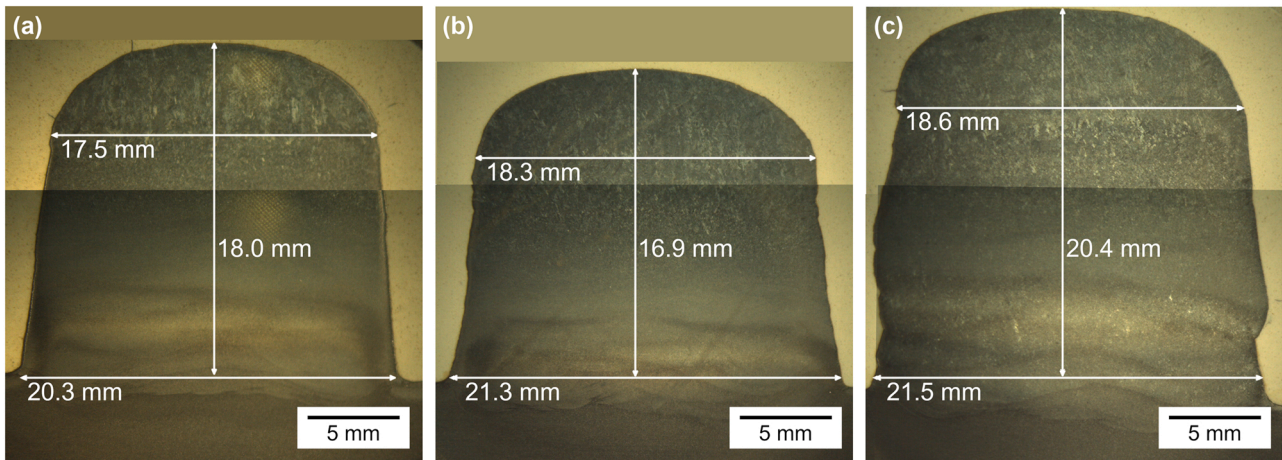


Fig. 20. SL-PTA MES built walls cross-sections ($w_s = 20$ mm): (a) layer height = 0.7 mm, $v_w = 6$ mm/s, (b) layer height = 1.3 mm, $v_w = 12$ mm/s, and (c) layer height = 2.3 mm, $v_w = 18$ mm/s.

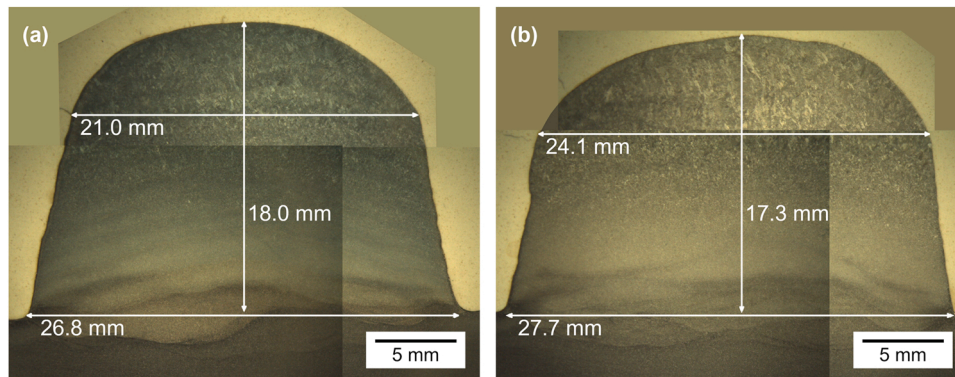


Fig. 21. SL-PTA MES built walls cross-sections ($w_s = 26.5$ mm): (a) 25% scanning speed at the edges and (b) 10% scanning speed at the edges.

width at both the bottom and the top. This indicates that SL energy distribution with more energy at the edges can contribute to reducing the width narrowing.

A possible explanation for this issue can be that the top surface of each layer was not flat but transformed into a camber-shaped top surface. As illustrated in Fig. 22, when the laser beam reached the edge of the cambered top surface, the laser beam was not vertical to the surface but with an angle. The interaction area of the laser beam was broadened due to the area sloping at the edges. The energy density was reduced because of the larger interaction area, and energy efficiency might be changed. Wettability was weakened at the edges, leading to the narrowing of the melt pool after each layer.

Fig. 23 shows the OM images taken from the six positions indicated in Fig. 8. The microstructure can be generally classified into pearlite (P),

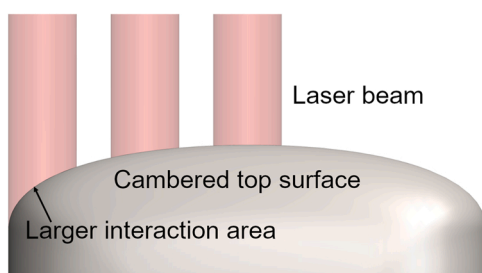


Fig. 22. The interaction area changed when the laser beam approached the edge of the cambered top surface.

polygonal ferrite (PF), acicular ferrite (AF) and bainite ferrite (BF). Lee et al. (2018) reported the formation of these microstructures as a function of cooling rate. PF is usually formed with slow cooling rates and relatively low strength. AF is characterised by fine and irregular-shaped grains alignment in arbitrary directions and has a good combination of strength and toughness. BF is usually transformed at low temperatures and rapid cooling rates with lath-type morphology and high dislocation density. The microhardness of BF is relatively high but brittle. Fig. 23a and b show the microstructures at the bottom of the Wall 3 cross-section. Air convection and less thermal cycling at the top position of the wall contributed to a fast cooling rate, which resulted in the formation of majorly BF and minorly PF microstructure. The half-height position of Wall 3, as presented in Fig. 23c and d, presents majorly AF and minorly PF microstructure. The cooling rate at the half-height position was slower than the top position due to longer thermal cycling, contributing to the formation of more AF and less BF. The prior austenite grain size shows no essential difference between the side and the centre of the wall at the half-height position. Fig. 23e and f show the OM images at the bottom of the Wall 3 cross-section closed to the fusion line, respectively at the centre and the side. Microstructure presents a majority of PF with minor P. Remelting and prolonged thermal cycling were the dominating factors at the bottom of the wall instead of convection and conduction to the base plate. Consequently, the cooling rate is the slowest at this position, which contributed to the forming of PF. Fig. 24a is the microhardness transition along the central line from the bottom to the top of the wall. Microhardness at the bottom is lower due to a higher content of PF. With the increase of AF and BF, microhardness rises to an average level of about 330 Hv and stays constant at the half-height and top

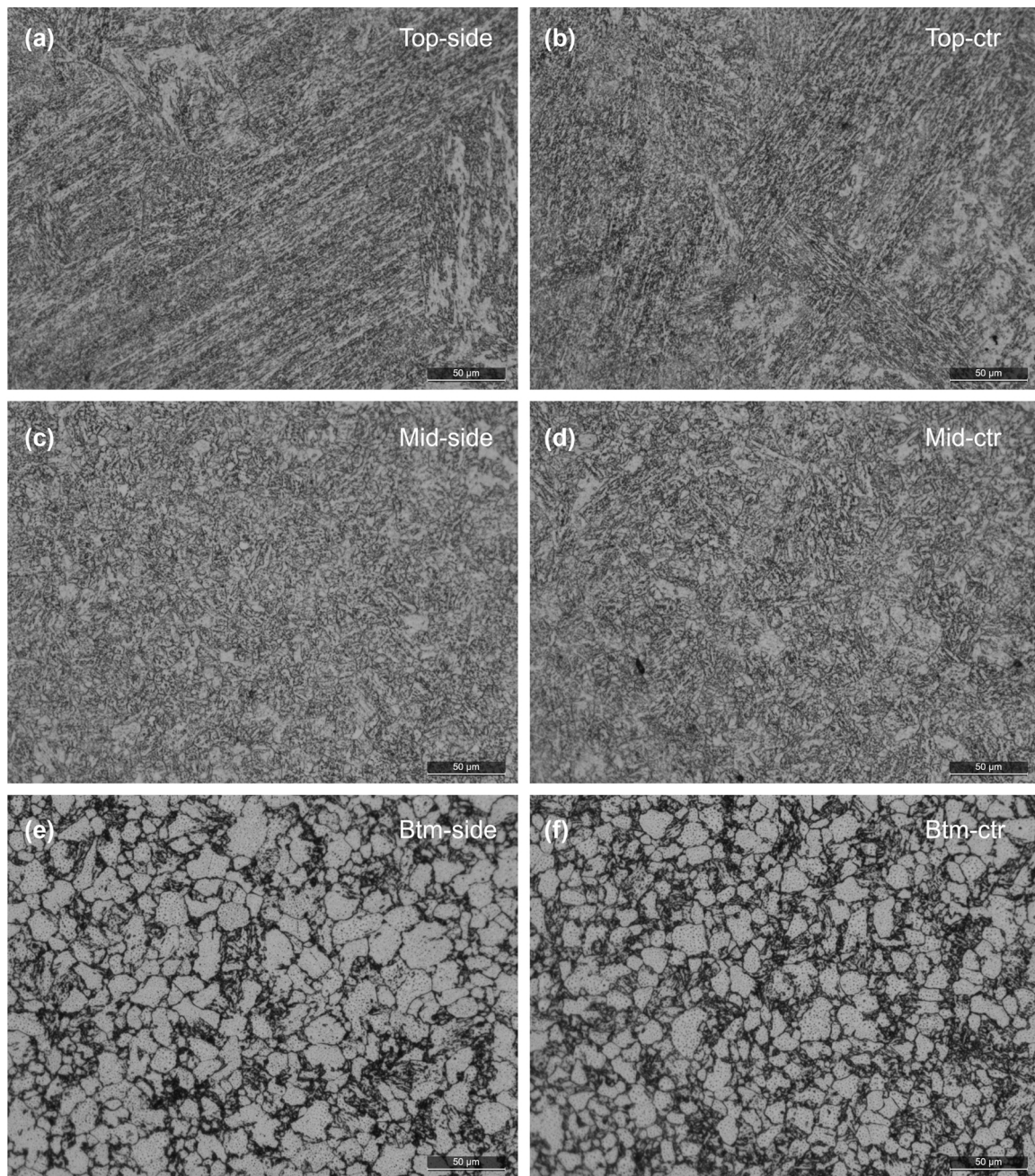


Fig. 23. OM images at different positions on the Wall 1 cross-section: (a) top-side, (b) top-centre, (c) middle-side, (d) middle-centre, (e) bottom-side, and (f) bottom-centre.

positions of the wall. Overall, no significant microstructure difference is shown between the centre and the side regions of the wall. This is further proved by the evenly distributed microhardness along the wall width (Fig. 24b), which is evidence that the SL did not affect the microstructure isotropy of the wall.

3.4. Future work

The MES method has the capability to reshape the melt pool and achieve a broad range of bead shapes with high accuracy. It has the potential to dynamically change the layer width and the layer height during the deposition by programming the scanning width, advancing speed and the wire feed speed. Layers with multi-section shapes can be easily deposited, and highly complex structures with near-net-shape can be built. Further studies are required to explore the capabilities of the

MES w-DED AM utilising a dynamic width changing SL. Also, higher build rates can be achieved through depositing very wide beads.

The mechanism of the width narrowing during the multi-layer deposition needs to be further studied and solved to achieve constant width for the part building. Therefore, understanding the mechanism behind this phenomenon is essential.

The MES can also contribute to the control of the thermal conditions independently of the bead geometry. In the conventional wire-based process, the energy input is difficult to adjust. Usually, in the conventional DED processes, a wider bead scale would lead to higher energy input and deeper penetration and affect the microstructure. The SL-PTA MES has the potential to control the energy input and improve the thermal gradient of the heat affect zone of the substrate and optimise the microstructure. The potential for independent thermal and geometry control should be studied as a mechanism to control the microstructure

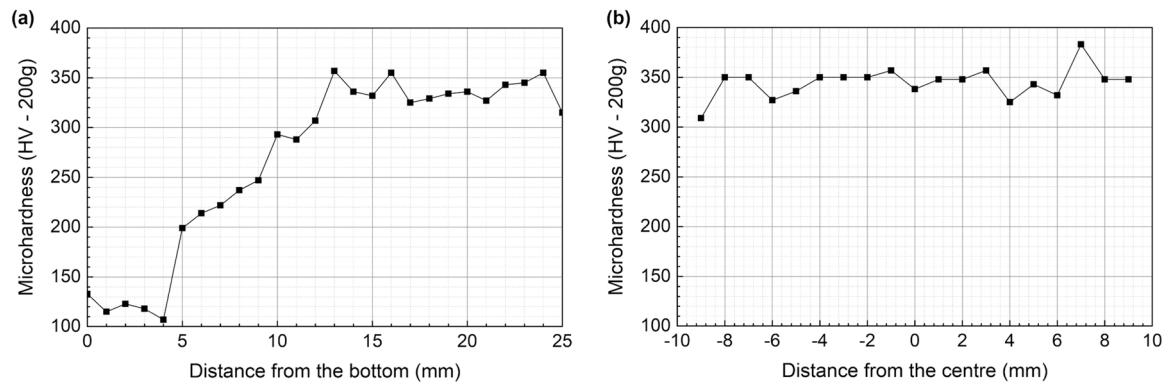


Fig. 24. Microhardness along two directions: (a) vertical and (b) horizontal.

and properties of deposited material.

4. Conclusions

1. In the MES system, a PTA can be employed to create an initial melt pool and melt the wire, and a SL can be used to reshape the melt pool and precisely control the bead width. By using MES, a w-DED AM process has been developed that enables independent control of the layer height and width over a wide range.
2. A bead shape control strategy can coordinate multiple parameters and control the bead shape systematically by using the wire feed speed to control layer height and the laser scanning width to control the layer width independent of each other. The advancing speed was adjusted in proportion to the scanning width to keep the same specific process energy of the SL.
3. The SL-PTA separation is a critical parameter to achieve a stable melt pool, thereby obtaining high-quality deposition without defects. Both a too close and a too far away SL-PTA distance might lead to defects.
4. Stable disposition can be achieved by adjusting the applied energy density across the scanning profile. More energy could be arranged at the edge to improve the spreading of the melt pool without increasing the total energy.
5. Multi-layer deposition can be achieved by MES w-DED process, which shows its potential in component fabrication. However, the layer width was reduced as more layers were deposited during the multi-layer wall building showing that further process studies are required.

Data Statement

Data underlying this study can be accessed through the Cranfield University repository at <https://doi.org/10.17862/cranfield.rd.19337438.v1>.

CRediT authorship contribution statement

Guangyu Chen: Conceptualization, Methodology, Validation, Formal analysis, Investigation, Resources, Data curation, Writing – original draft, Visualization. **Stewart Williams:** Conceptualization, Methodology, Resources, Writing – review & editing, Supervision, Project administration, Funding acquisition. **Jialuo Ding:** Conceptualization, Methodology, Resources, Writing – review & editing, Supervision, Project administration, Funding acquisition. **Chong Wang:** Investigation, Writing – review & editing. **Wojciech Suder:** Investigation, Resources.

Declaration of Competing Interest

The authors declare the following financial interests/personal relationships which may be considered as potential competing interests: Guangyu Chen reports financial support was provided by China Scholarship Council. Stewart Williams reports financial support was provided by Engineering and Physical Sciences Research Council. Stewart Williams has patent #Additive Manufacture (GB2569673) issued to Cranfield University. Wojciech Suder has patent #Additive Manufacture (GB2569673) issued to Cranfield University.

Acknowledgements

Guangyu Chen would like to express his gratitude to Cranfield University, United Kingdom and China Scholarship Council, China (No. 201706680064) for funding his research studies. The authors would like to thank New Wire Additive Manufacturing (NEWAM), United Kingdom (EP/R027218/1) programme for financial support. The authors also would like to thank Flemming Nielsen, Nisar Shah, John Thrower, and Steve Pope for the technical support. The authors also appreciate the support from Jun Wang on the microstructure analysis.

References

- Abioye, T.E., Folkes, J., Clare, A.T., 2013. A parametric study of Inconel 625 wire laser deposition. *J. Mater. Process. Technol.* 213. <https://doi.org/10.1016/j.jmatprot.2013.06.007>.
- Cai, C., Li, L., Tao, W., Chen, X., 2017. Effects of weaving laser on scanning laser-MAG hybrid welding characteristics of high-strength steel. *Sci. Technol. Weld. Join.* 22. <https://doi.org/10.1080/13621718.2016.1199126>.
- DebRoy, T., Wei, H.L., Zuback, J.S., Mukherjee, T., Elmer, J.W., Milewski, J.O., Beese, A.M., Wilson-Heid, A., De, A., Zhang, W., 2018. Additive manufacturing of metallic components – Process, structure and properties. *Prog. Mater. Sci.* <https://doi.org/10.1016/j.pmatsci.2017.10.001>.
- Ding, D., Pan, Z., Cuiuri, D., Li, H., 2015. Wire-feed additive manufacturing of metal components: technologies, developments and future interests. *Int. J. Adv. Manuf. Technol.* <https://doi.org/10.1007/s00170-015-7077-3>.
- Dinovitzer, M., Chen, X., Laliberte, J., Huang, X., Frei, H., 2019. Effect of wire and arc additive manufacturing (WAAM) process parameters on bead geometry and microstructure. *Addit. Manuf.* 26. <https://doi.org/10.1016/j.addma.2018.12.013>.
- Hao, K., Li, G., Gao, M., Zeng, X., 2015. Weld formation mechanism of fiber laser oscillating welding of austenitic stainless steel. *J. Mater. Process. Technol.* 225. <https://doi.org/10.1016/j.jmatprot.2015.05.021>.
- Lee, S.I., Lee, S.Y., Lee, S.G., Jung, H.G., Hwang, B., 2018. Effect of strain aging on tensile behavior and properties of API X60, X70, and X80 pipeline steels. *Met. Mater. Int.* 24. <https://doi.org/10.1007/s12540-018-0173-9>.
- Li, R., Wang, G., Ding, Y., Tang, S., Chen, X., Dai, F., Wang, R., Song, H., Zhang, H., 2020. Optimisation of the geometry for the end lateral extension path strategy to fabricate intersections using laser and cold metal transfer hybrid additive manufacturing. *Addit. Manuf.* 36. <https://doi.org/10.1016/j.addma.2020.101546>.
- Liang, Y., Hu, S., Shen, J., Zhang, H., Wang, P., 2017. Geometrical and microstructural characteristics of the TIG-CMT hybrid welding in 6061 aluminum alloy cladding. *J. Mater. Process. Technol.* 239. <https://doi.org/10.1016/j.jmatprot.2016.08.005>.
- Liu, M., Ma, G., Liu, D., Yu, J., Niu, F., Wu, D., 2020. Microstructure and mechanical properties of aluminum alloy prepared by laser-arc hybrid additive manufacturing. *J. Laser Appl.* 32. <https://doi.org/10.2351/7.0000082>.

- Martina, F., Mehnert, J., Williams, S.W., Colegrove, P., Wang, F., 2012. Investigation of the benefits of plasma deposition for the additive layer manufacture of Ti-6Al-4V. *J. Mater. Process. Technol.* 212. <https://doi.org/10.1016/j.jmatprotec.2012.02.002>.
- Mok, S.H., Bi, G., Folkes, J., Pashby, I., 2008. Deposition of Ti-6Al-4V using a high power diode laser and wire, part I: investigation on the process characteristics. *Surf. Coat. Technol.* 202. <https://doi.org/10.1016/j.surfcoat.2008.02.008>.
- Montagu, J., 2018. Galvanometric and resonant scanners. In: *Handbook of Optical and Laser Scanning*. <https://doi.org/10.1201/9781315218243-8>.
- Qian, Y.P., Huang, J.H., Zhang, H.O., Wang, G.L., 2008. Direct rapid high-temperature alloy prototyping by hybrid plasma-laser technology. *J. Mater. Process. Technol.* 208. <https://doi.org/10.1016/j.jmatprotec.2007.12.116>.
- Schulz, M., Klocke, F., Riepe, J., Klingbeil, N., Arntz, K., 2019. Process optimisation of wire-based laser metal deposition of titanium. *J. Eng. Gas Turbines Power* 141. <https://doi.org/10.1115/1.4041167>.
- Sequeira Almeida, P.M., Williams, S., 2010. Innovative process model of Ti-6Al-4V additive layer manufacturing using cold metal transfer (CMT), in: 21st Annual International Solid Freeform Fabrication Symposium - An Additive Manufacturing Conference, SFF 2010.
- Wang, C., Suder, W., Ding, J., Williams, S., 2021a. Wire based plasma arc and laser hybrid additive manufacture of Ti-6Al-4V. *J. Mater. Process. Technol.* 293. <https://doi.org/10.1016/j.jmatprotec.2021.117080>.
- Wang, C., Suder, W., Ding, J., Williams, S., 2021b. Bead shape control in wire based plasma arc and laser hybrid additive manufacture of Ti-6Al-4V. *J. Manuf. Process.* 68. <https://doi.org/10.1016/j.jmapro.2021.07.009>.
- Wang, C., Suder, W., Ding, J., Williams, S., 2021c. The effect of wire size on high deposition rate wire and plasma arc additive manufacture of Ti-6Al-4V. *J. Mater. Process. Technol.* 288. <https://doi.org/10.1016/j.jmatprotec.2020.116842>.
- Yang, D., Wang, G., Zhang, G., 2017. A comparative study of GMAW- and DE-GMAW-based additive manufacturing techniques: thermal behavior of the deposition process for thin-walled parts. *Int. J. Adv. Manuf. Technol.* 91. <https://doi.org/10.1007/s00170-016-9898-0>.
- Yehorov, Y., da Silva, L.J., Scotti, A., 2019. Balancing WAAM production costs and wall surface quality through parameter selection: a case study of an Al-Mg5 alloy multilayer-non-oscillated single pass wall. *J. Manuf. Mater. Process.* 3. <https://doi.org/10.3390/jmmp3020032>.
- Zhang, H.O., Qian, Y.P., Wang, G.L., 2006. Study of rapid and direct thick coating deposition by hybrid plasma-laser manufacturing. *Surf. Coat. Technol.* 201. <https://doi.org/10.1016/j.surfcoat.2006.02.049>.